Yujiong Liu
Robotics and Mechatronics Lab,
Department of Mechanical Engineering,
Virginia Tech,
Blacksburg, VA 24061
e-mail: yjliu@vt.edu

Jiamin Wang
Department of Mechanical Engineering,
Virginia Tech,
Blacksburg, VA 24061
e-mail: jmechw@vt.edu

Pinhas Ben-Tzvi[1]
Mem. ASME
Robotics and Mechatronics Lab,
Department of Mechanical Engineering,
Virginia Tech,
Blacksburg, VA 24061
e-mail: bentzvi@vt.edu

A Cable Length Invariant Robotic Tail Using a Circular Shape Universal Joint Mechanism

This paper presents the development of a new robotic tail based on a novel cable-driven universal joint mechanism. The novel joint mechanism is synthesized by geometric reasoning to achieve the desired cable length invariance property, wherein the mechanism maintains a constant length for the driving cables under universal rotation. This feature is preferable because it allows for the bidirectional pulling of the cables which reduces the requisite number of actuators. After obtaining this new joint mechanism, a serpentine robotic tail with fewer actuators, simpler controls, and a more robust structure is designed and integrated. The new tail includes two independent macro segments (2 degrees of freedom each) to generate more complex shapes (4 degrees of freedom total), which helps with improving the dexterity and versatility of the robot. In addition, the pitch bending and yaw bending of the tail are decoupled due to the perpendicular joint axes. The kinematic modeling, dynamic modeling, and workspace analysis are then explained for the new robotic tail. Three experiments focusing on statics, dynamics, and dexterity are conducted to validate the mechanism and evaluate the new robotic tail's performance.
[DOI: 10.1115/1.4044067]

1 Introduction

In nature, animals use tails for a variety of tasks ranging from stabilization (Kangaroo [1]), maneuvering (Cheetah [2]), propulsion (Fish [3]), and manipulation (Monkey [4]). Inspired by these amazing functionalities, researchers recently devoted significant effort toward investigating the dynamical effects of tails on mobile platforms both theoretically [5–10] and practically [11–16]. Focusing on its functionality as a manipulator, a tail is essentially a flexible onboard serial manipulator which has been investigated and widely used for decades [17–19]. Based on the system complexity, existing robotic tails can be categorized into three classes: the simplest and most commonly used pendulum tails [11–16], the more complicated serpentine tails [20–23], and the most complex elastic continuum tails [17–19,24]. For more thorough state of the art review, see Ref. [25] and the references therein.

From the perspective of the tail's dynamical functions for maneuvering and stabilization, a pendulum was believed to be the most efficient way to generate dynamic loading. However, recent research [9,22] revealed that serpentine type tails have the benefit of generating higher inertia loading in comparison with their pendulum counterparts. In addition, continuum tails are known to have the advantages of being compliant to obstacles, being more dexterous, and having larger workspace. Therefore, although pendulum tails are widely used, serpentine and continuum tails are being researched more extensively.

In nature, most animal tails consist of serially connected 2 degrees of freedom (DOFs) joints (the spine joints). Therefore, a reasonable biomimetic robotic tail can also be constructed with multiple serially connected 2-DOF joints—a universal joint with pitch and yaw DOFs. However, to drive a universal joint by cable, three actuators are usually required due to the pull-only property of cables. For instance, the recently developed universal spatial robotic tail (USRT) [21] as well as cable-driven robotic wrists/manipulators [26–28] use three actuators to drive the universal joint. Using three actuators to drive the 2-DOF joint results in an over-actuated system where one actuator is always passive and redundant, which may greatly increase the difficulty of the actuation control through cable tension.

To avoid this disadvantage, one way to reduce actuation for cable-driven joints is shown in the discrete modular serpentine robotic tail (DMST) design [20]. For the DMST, the authors designed specific circular cable routing paths to guarantee the bidirectional pulling of the actuators. However, this approach only works well for planar revolute joints. The work did not generalize this mechanism to a spatial case (a spatial cable routing profile for the more general universal joint).

Another potential solution is found in a minimally invasive surgical device [19] and a robotic wrist [29]. In these two papers, the authors illustrate the idea that by replacing the commonly used pivots or continuum backbone by specifically designed rolling joints, the manipulator is able to achieve specific cable length features (for the case of Ref. [19], the desired feature is the asymmetric cable length behavior so that the manipulator stiffness is variable). Although the variable stiffness is usually not a primary consideration in robotic tails, the innovative idea that appeared in Refs. [19,29] could lead to a potential solution for the problem stated above.

Following the same idea as shown in the DMST, this paper aims to find its spatial analog. Due to the complexity of spatial mechanisms, a more strict and theoretical method is required to synthesize this mechanism. Geometric approaches have been widely used in mechanism research, both in analysis [30] and synthesis [31], and it is especially suitable for a symmetric mechanisms. Therefore, in this paper, a geometric reasoning approach is proposed to carry out the mechanism synthesis procedure.

In summary, this work is motivated by the need for a new cable-driven joint to develop a spatial serpentine tail with a minimal number of actuators. Under spherical geometry and universal rotation assumptions, the lowest level of actuation can be achieved to maintain the cable length's invariance property introduced in this paper. To meet this property, a new joint is synthesized by geometric reasoning. A universal joint with perpendicular circular shapes satisfies the invariance property. Based on this new joint, a new robotic tail was developed with fewer actuators, simpler control, and a more robust structure as shown in Fig. 1. Like other continuum/serpentine robotic tails, this new tail design has a large end effector workspace and variable center of mass (COM), which makes it suitable as both an onboard flexible manipulator and a

[1]Corresponding author.

Contributed by the Mechanisms and Robotics Committee of ASME for publication in the Journal of Mechanisms and Robotics. Manuscript received December 3, 2018; final manuscript received June 12, 2019; published online July 9, 2019. Assoc. Editor: Alon Wolf.

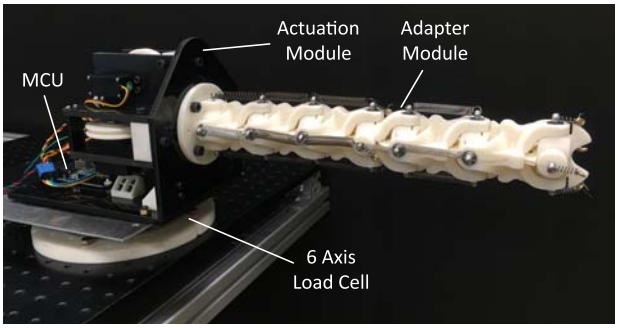

Fig. 1 RML tail prototype

dynamical reaction appendage for a mobile platform such as a quadruped. In addition, the new unique joint mechanism can potentially be applied to cable-driven robotic wrists as well as broader cable-driven manipulators.

This paper is organized as follows: The first section briefly reviews the state of the art of robotic tail research and describes the motivation of this work. Section 2 goes into details to present the background of this research that how the idea was concieved. Guided by the new idea, Sec. 3 describes a geometric reasoning process to synthesize the desired cable-driven universal joint. Section 4 substantiates this new mechanism and presents the mechanical design and system integration of the new robotic tail. Section 5 provides the kinematic, dynamic, and workspace analysis for the new robotic tail. Lastly, the experiments are discussed in Sec. 6 to validate the new mechanism and quantify its performance.

2 Cable Length Invariance Challenge for Spatial Mechanisms

As shown in Figs. 2(*a*)–2(*c*), three cable-driven serpentine tails were developed in the literature to achieve spatial motion of tails. The USRT (Fig. 2(*a*)) [21] design applies the cable-driven flexible manipulator concept [17,18] and has the same advantages; it is compliant to obstacles due to the elastic backbone and is able to generate the rolling motion by combining yaw bending and pitch bending. However, as shown in Fig. 2(*d*), for a cable-driven universal joint with straight cable routing, due to the pull-only property of cables, at least three actuated cables are required although one of them is always passive. This leads to a significant disadvantage of such systems in a manner that one actuator is not active. This disadvantage is caused by the unequal shortening/lengthening lengths of cable during universal joint rotation (or universal rotation), i.e., $\Delta_1 \neq \Delta_2 \neq \Delta_3$. Therefore, to address this shortcoming, the DMST (Fig. 2(*b*)) [20] tail design was proposed. Circular segment shapes are utilized to guarantee the equal shortening/lengthening lengths of the cables during planar rotation, i.e., $\Delta_R = \Delta_L$ in Fig. 2(*f*) (as a comparison, Fig. 2(*e*) illustrates the case of planar straight cable routing). This property enables DMST to use one pulley to drive the cable in both directions, which reduces the number of total required actuators (DMST has 2 DOFs with one for planar bending and one for overall rolling). R3RT (Fig. 2(*c*)) [22] realized the same idea as in DMST but used gears to replace the separate driven cables and included another planar bending DOF, which improves the reliability, dexterity, and the workspace of the robot. However, this idea was only successful in the planar case which limits the mobility of the DMST/R3RT to be the same as the mobility of the USRT. A spatial mechanism that has the same mobility as the USRT but uses one pulley to drive both cable directions had not been found. The challenge lies in the difficulty of determining the proper spatial cable routings that guarantee equally shortening/lengthening of cables for the spatial motion (universal rotation in this paper).

To address this challenge, it is necessary to identify the conditions under which the cables shorten and lengthen equally for universal rotation. As long as these conditions are identified, the desired spatial cable routing and mechanism would be synthesized accordingly. This leads to the cable length invariance concept.

Before discussing the cable length invariance concept, the cable routing profile terminology needs to be defined first. A cable routing

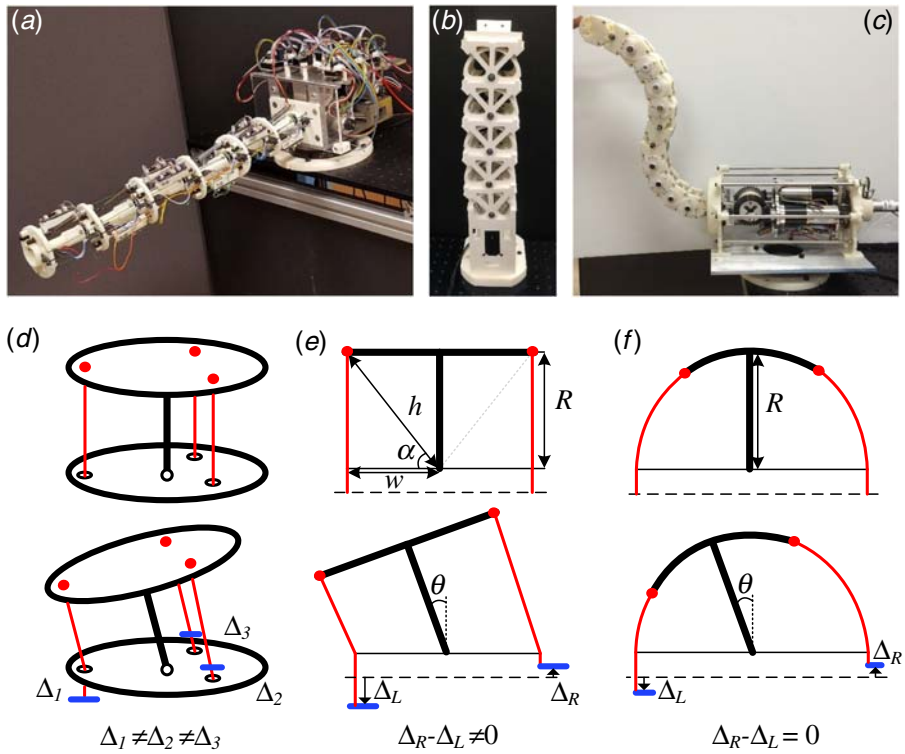

Fig. 2 (*a*) USRT, (*b*) DMST, (c) R3RT, (*d*) spatial straight routing, (e) planar straight routing, and (*f*) planar circular routing

profile is a smooth curve on a smooth rigid body surface where the cable length along the cable routing profile is the line integral of the curve. Due to the pull-only property of cables, a cable-driven system usually uses two cables to drive the back and forth motions of one joint. Therefore, a cable-driven system is said to possess cable length invariance property if for each pair of cables, constrained by their corresponding cable routing profiles, the lengthened length of one cable equals to the shortened length of the other cable (for instance, $\Delta_R = \Delta_L$ in Fig. 2(*f*)) during any permissible motions of the system. This is equivalent to keeping the total length of each pair of cables constant.

With the proper definition of the cable length invariance property, the challenges may be stated as (1) identifying the conditions of a cable-driven universal joint that achieves the cable length invariance property, (2) synthesizing this joint based on these conditions, and (3) designing the spatial robotic tail based on this new joint. The robotic tail should also possess the cable length invariance property throughout the whole system.

3 Mechanism Syntheses Based on Geometric Reasoning

With these challenges in mind, this section applies geometric reasoning to identify the conditions and synthesizes the desired joint mechanism. Since frictionless, massless, tensioned cables tend to find the shortest path, the terminology "geodesic" is used in this paper. A geodesic is defined as the shortest path connecting two points on a manifold. For instance, on a sphere, the geodesic is the short arc of the corresponding great circle. In this paper, the geodesic connecting points A and B is denoted by g_{AB} with length $l(g_{AB})$. The corresponding central angle is denoted by $\angle A\hat{O}B$, representing the central angle starting from point A, ending at point B, and centered at point O and its complementary angle is denoted by $\angle A\check{O}B = 2\pi - \angle A\hat{O}B$. In addition, as discussed in Sec. 2, this paper focuses on the "universal rotation" that is defined by two consecutive elementary rotations with respect to x and y'.

For the planar case, as shown in Fig. 2(*f*), the circular cable routing profile is a simple and efficient solution for achieving cable length invariance. However, for the universal rotation case, the cable routing profile design problem becomes challenging. This is due to the dependency of the two rotations in the universal joint. Therefore, a careful theoretical analysis should be conducted first. Since a sphere is the spatial analog of a circle, we assume that the two rigid bodies are both spheres. Then, as shown in Fig. 3(*a*), the problem is formulated as: given spherical objects A and B that are connected by a universal joint, finding two cable routing profiles such that their lengths both remain invariant under the universal rotation. The triangles in Fig. 3(*a*) represent the anchor points for cable routing. Note that Fig. 3(*a*) only shows one set of cable routing profiles (the cables go from anchor 1 to 2 and from anchor 3 to 4) and four anchors. The actual anchor number and their positions are determined in the following detailed analysis.

To simplify the analysis, let us first consider the case with only one set of cables. When the moving rigid body undergoes universal rotation, what is the condition of achieving cable length invariance? These conditions are given by the following theorem. However, to prove this theorem, an important observation is required first.

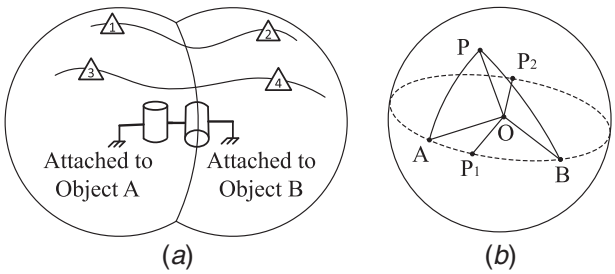

Fig. 3 (*a*) Illustration of problem setting for mechanism syntheses and (*b*) the geometric illustration of the lemma

LEMMA. *For two fixed points A and B and a moving point P on a sphere $\mathcal{S}_O$ centered at O, $l(g_{AP}) + l(g_{BP})$ remains constant if and only if line segment AB goes through O.*

Proof. The sufficient part is straightforward. Since AB goes through center O, g_{AP} and g_{BP} constitute a half great circle which has a total length of $l(g_{AP}) + l(g_{BP}) = r\pi$. r is the radius of the sphere. For the necessary part, because of $l(g_{AP}) + l(g_{BP}) = r\angle P\hat{O}A + r\angle P\hat{O}B = r(\angle P\hat{O}A + \angle P\hat{O}B)$, we just need to find the condition to make $\angle P\hat{O}A + \angle P\hat{O}B$ constant. Let the circle Cir_{OAB} be the great circle going through points A and B (the dotted circle in Fig. 3(*b*)). Because P is able to move, we choose two specific positions of P, namely, P_1 and P_2, where P_1 is on the short arc of Cir_{OAB} between A and B and P_2 is on the long arc. Therefore, $\angle P_1\hat{O}A + \angle P_1\hat{O}B = \angle A\hat{O}B$ and $\angle P_2\hat{O}A + \angle P_2\hat{O}B = \angle A\check{O}B$. To make $\angle P\hat{O}A + \angle P\hat{O}B$ constant, $\angle A\hat{O}B$ should be equal to $\angle A\check{O}B$, i.e., $\angle AOB = \pi$. ∎

Since one moving point does not reflect the universal rotation of a rigid body, we now consider the case with two moving points.

THEOREM. *For two fixed points A and B on a sphere $\mathcal{S}_O$ and two fixed points P_1 and P_2 on a rigid body $\mathcal{T}$ that rotates universally around O, if P_1 and P_2 are also chosen to be on $\mathcal{S}_O$ and on the great circle Cir_{OAB} going through A and B, then $l(g_{AP_1}) + l(g_{BP_2})$ remains constant if and only if line segment AB coincides with the first rotation axis x of the universal joint and the second rotation axis y' is perpendicular to Cir_{OAP_1}.*

Proof. The sufficient part is relatively simple. Since segment AB coincides with axis x, under the first rotation, A, B, P_1, and P_2 remain on a half great circle. Since axis y' is perpendicular to Cir_{OAB}, the second rotation makes P_1 and P_2 slide along the half great circle. Thus, $l(g_{AP_1}) + l(g_{BP_2})$ remains constant.

The necessary part is achieved by considering three specific scenarios. The *first scenario* is to move $g_{P_1P_2}$ so that g_{AP_1} and $g_{P_1P_2}$ are always in the same plane, i.e., A, P_1, and P_2 on the same geodesic. From the above lemma, AB has to go through O to guarantee the length invariance, as the AB' shown in Fig. 4(*a*). The *second scenario* is to rotate only one axis of the universal joint, say the x axis. Figure 4(*b*) depicts this scenario. P_1 is chosen to be on the great circle which is perpendicular to the rotation axis EF (the x axis) and OP_1 is perpendicular to the circle going through both the line EF and the line AB. P_2 is chosen to coincide with B. Therefore, if $g_{P_1P_2}$ rotates $\pm\pi/2$, then P_1 goes to P_1' $(\pi/2)$ and P_1'' $(-\pi/2)$, respectively, and P_2 goes to P_2' $(\pi/2)$ and P_2'' $(-\pi/2)$, respectively. Obviously, $l(g_{BP_2'}) = l(g_{BP_2''})$ and $l(g_{AP_1'}) - l(g_{AP_1''}) = 2r\angle A\hat{O}E$. Thus, to make $l(g_{AP_1'}) = l(g_{AP_1''})$, $\angle A\hat{O}E$ has to be either 0 or $\pi/2$, i.e., line AB should either coincide with or be perpendicular to the rotation axis. However, considering the other rotation of the universal joint, the perpendicular case is not valid. Figure 4(*c*) shows such a counterexample. In Fig. 4(*c*), EF is the first rotation axis, GH is the second rotation axis, A, B, P_1, and P_2 are all in the perpendicular plane of line EF. The first rotation makes P_1 coincide with G. This specific position allows P_1 to remain in its position under the second rotation which moves from P_2 to P_2'. P_2'' is the point on $g_{BP_2'}$ that has the same length as g_{BP_2}. Therefore, $l(g_{BP'_2}) \neq l(g_{BP_2})$. As for the necessity of y' being perpendicular to Cir_{OAP_1}, *the third scenario* is constructed. As shown in Fig. 4(*d*), AB coincides with the x axis. GH is on the y' axis. Cir_{OAM} lies in the perpendicular plane of GH where M is the midpoint of the half great circle from A to B. P_1 is chosen to coincide with A and $\angle P_1\hat{O}P_2 = \pi/2$. P_2 is chosen to have the central angle $\angle P_2\hat{O}M = \theta$. Rotating $g_{P_1P_2} - \pi/2$ with respect to GH maps P_1 to P_1' and P_2 to P_2'. Thus, before rotating, $l(g_{AP_1}) + l(g_{BP_2}) = r\pi$. After rotating, $l(g_{AP_1'}) + l(g_{BP_2'}) = r((\pi/2) + (\pi/2) + \theta)$. Therefore, to guarantee length invariance, $\theta = 0$. Combining the three scenarios completes the necessary part of the proposition. Combining the sufficient and necessary part completes the theorem proof. ∎

This theorem provides the conditions to achieve length invariance on a sphere. That is, the cable must go through the pivots of the rotation axis. Therefore, for the two sets of the cable case, each set should go through one of the two rotation axes of the universal joint. The bellow corollary validates this approach. Note that

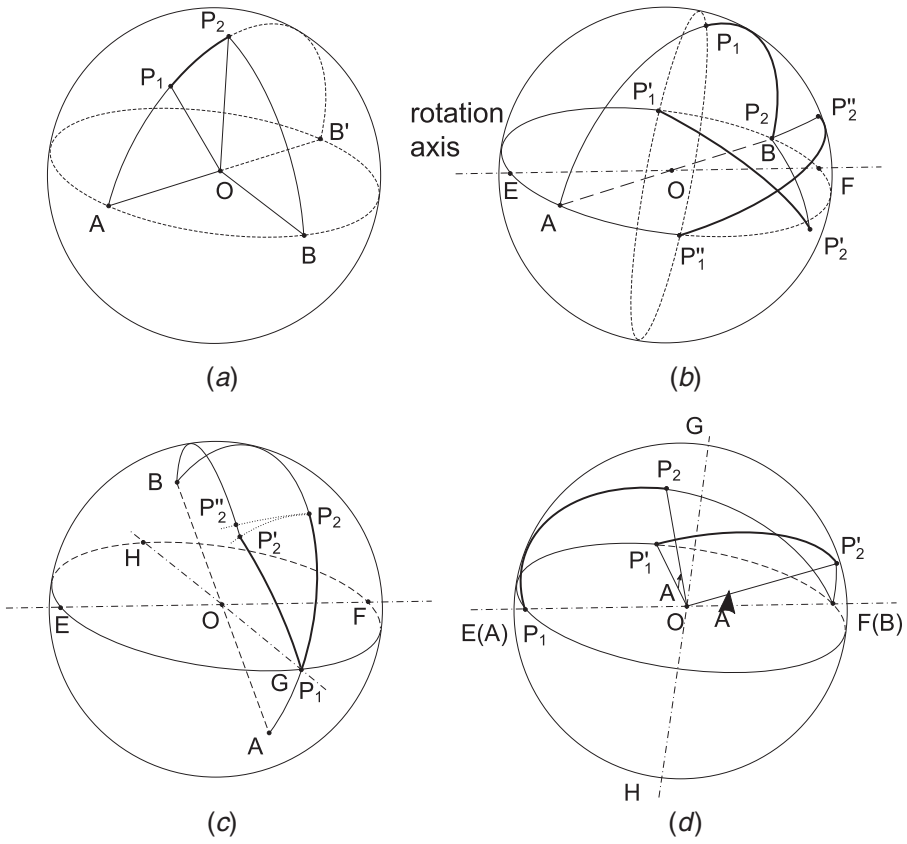

Fig. 4 One cable set routing case: (*a*) the first scenario in the theorem requires *B* to coincide with *B′*, (*b*) the second scenario in the theorem, (c) an example showing that *AB* cannot be perpendicular to the first rotation axis *EF*, and (*d*) the third scenario in the theorem

since the theorem also requires the perpendicularity between the rotation axis and the half circle Cir_{OAP_1}, the second rotation axis in the universal joint has to be perpendicular to the first one.

COROLLARY. *For the cable-driven mechanism shown in Fig. 5, AB and GH are two perpendicular rotation axes of a universal joint. P_1 is the midpoint of the half great circle Cir_{OGP_1} from G to H. P_2 is the midpoint of the half great circle Cir_{OAP_2} from A to B. Define two cable routing profiles from P_1 to P_2 where one profile consists of g_{P_1A}, g_{AP_2}, g_{P_2B}, and g_{BP_1} and the other consists of g_{P_1G}, g_{GP_2}, g_{P_2H}, and g_{HP_1}. For such a mechanism, both profiles maintain length invariance under the universal rotation.*

Proof. Since P_1 is the midpoint of the half great circle Cir_{OGP_1} from G to H, GH is perpendicular to Cir_{OAP_1}. From the theorem, $l(g_{AP_1}) + l(g_{BP_1})$ keeps constant. Actually, g_{AP_1} and g_{BP_1} constitute a half great circle. $l(g_{AP_1}) + l(g_{BP_1}) = \pi r$. The same holds for g_{GP_2} and g_{HP_2}. It is clear that the first cable routing profile (consisting of g_{P_1A}, g_{AP_2}, g_{P_2B}, and g_{BP_1}) constitutes two half great circles. Thus, its length remains at $2\pi r$. The same holds for the second cable routing profile (consisting of g_{P_1G}, g_{GP_2}, g_{P_2H}, and g_{HP_1}). ■

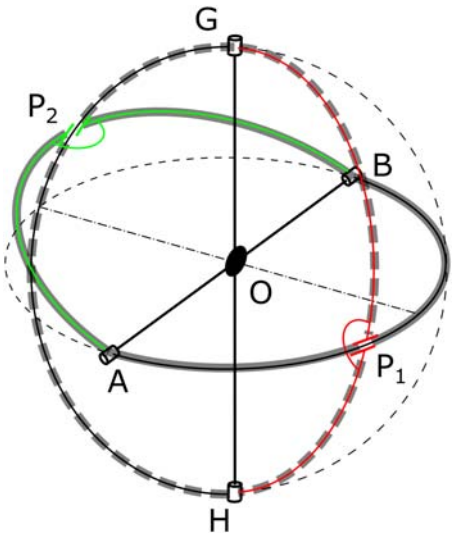

Fig. 5 The illustration of the two sets of the cable case. The lines from G to H through P_1 belong to one solid body. The lines from A to B through P_2 belong to another solid body. The transparent thick solid lines belong to one cable routing profile. The transparent thick dashed lines belong to the other cable routing profile.

This corollary essentially provides the building blocks for more complicated mechanisms. For instance, if we connect this block serially, we are able to construct the tail we are looking for in this paper. For this case, the only requirement is to fuse one of the moving point P_1 or P_2 to the moving points on another block, as shown in Fig. 6. Since the two connecting blocks are independent, the angle between the two sliding circles (the contacting half circles $\mathrm{Cir}_{O_1A_1P_3}$ and $\mathrm{Cir}_{O_2A_2P_3}$ in Fig. 6) can be any angle. Figure 6 shows two typical connection angles: 0 and $\pi/2$. Note the fusion of the moving point P_1 or P_2 does not imply that the contact of the two blocks has to be a point. In practice, larger contacting area has better mechanics properties.

4 Prototype Design and Integration

The mathematical reasoning in Sec. 3 provides the foundation upon which to construct the robotic tail. The tail design can be realized by developing the mechanisms into serially connected joint segments, incorporating elastic elements into the mechanical system, and integrating the whole system with actuations. The tail heretofore named the RML (Robotics and Mechatronics Lab) tail.

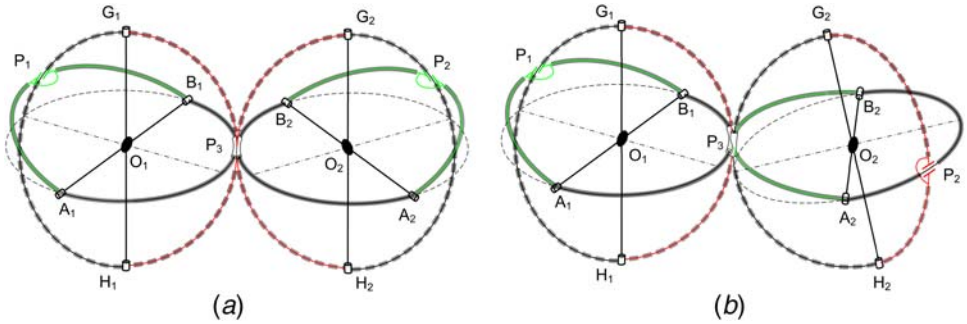

Fig. 6 Two typical connecting cases: (*a*) the sliding circle $Cir_{O_1A_1P_3}$ is parallel to the other sliding circle $Cir_{O_2A_2P_3}$, (*b*) the sliding circle $Cir_{O_1A_1P_3}$ is parallel to the other sliding circle $Cir_{O_2G_2P_3}$. The transparent thick solid lines belong to one cable routing profile. The transparent thick dashed lines belong to the other cable routing profile.

Section 4.1 summarizes the overall design of RML tail, and Secs. 4.2–4.5 detail the specific components of the tail.

4.1 Robot Structure and Modularity. The overall view of the whole robotic tail is shown in Fig. 7. The whole system consists of two macro segments and one actuation module. Each macro segment consists of several sub-segments and can provide 2-DOF bending independently, namely, yaw and pitch. Therefore, the robotic tail in Fig. 7 is able to achieve a 4-DOF bending motion in total, which requires four actuators in the actuation module. As in the USRT, the rolling motion can be achieved by combining the yaw bending and the pitch bending. Note that the housing module is counted into the macro segment 1 and the adapter module into macro segment 2, respectively, as they are the start points for the subsequent macro segments.

For each macro segment, two sets of cables are required to drive the bidirectional motion of both yaw and pitch bending. As shown in Fig. 7, for example, of segment 1, the cables on the top and bottom belong to one set (cable set A) while the cables in the front and back (not visible in the figure) belong to another set (cable set B). Thus, based on the cable length invariance property, both cable set A and cable set B keep a constant total length during motion.

The design is intended to achieve modularity so that the tail can be extended easily. In addition, modularity facilitates manufacturing as well as enhances the exchangeability of parts. Therefore, each segment module is designed to be as symmetric as possible. The tail itself consists of four modules, as shown in Fig. 7. Module A and module B, constituting an individual segment, are the most important modules since they serve as the backbone of the tail. For the current design of the segment, module B is able to rotate ±30 deg with respect to module A. This allows a ±90 deg bending (pitch) in total for the first macro segment and a ±180 deg bending (yaw) in total for the entire tail. The adapter module, as the name shows, serves as adapter from the previous macro segment to the next macro segment. Therefore, the adapter module can be partitioned in the middle with the first half connecting with module A and the second with module B, respectively. Another important function of the adapter module is to distribute the cables emanating from the center hole of the previous macro segment to drive the following macro segment. Section 4.3 will discuss in more detail the adapter module and the macro segment cable routing. The housing module is used to connect the first macro segment to the actuation module; thus, it is only adopted once in the structure.

At the end of each cable, a pretightening spring and a cable terminal are designed to ensure cable tension. Between adjacent eyebolts, extensional springs (hidden in Fig. 7 to have a better view of cable routing) are utilized to compensate gravity and backbone elasticity.

4.2 Segment Design. The segment was designed to realize the mechanism synthesized in Sec. 3. That is, the two sets of cables in the segment should maintain the same cable routing profile as in

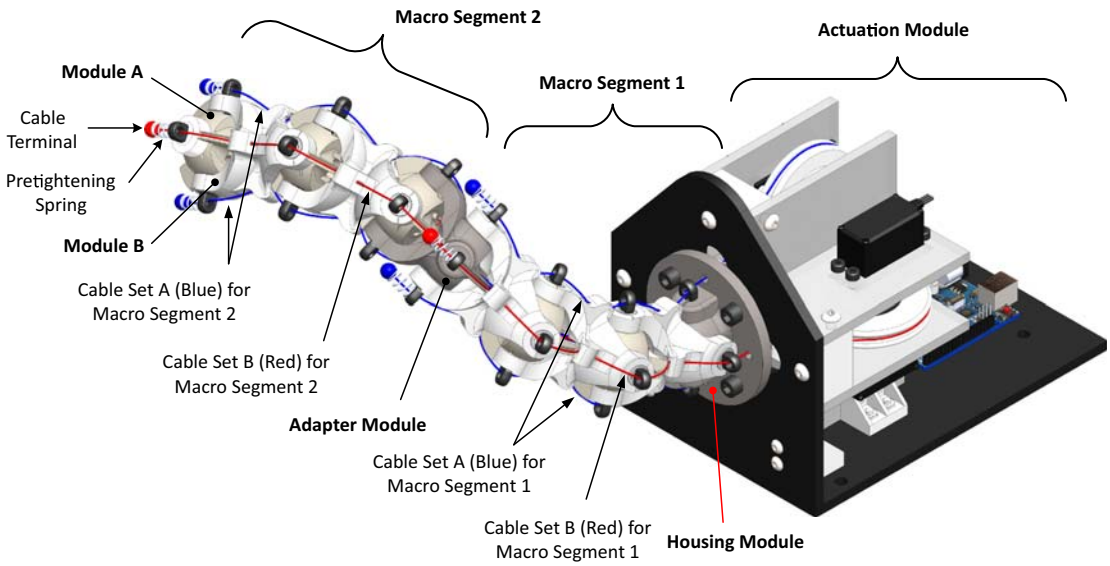

Fig. 7 Complete assembly of the RML tail without the extensional springs

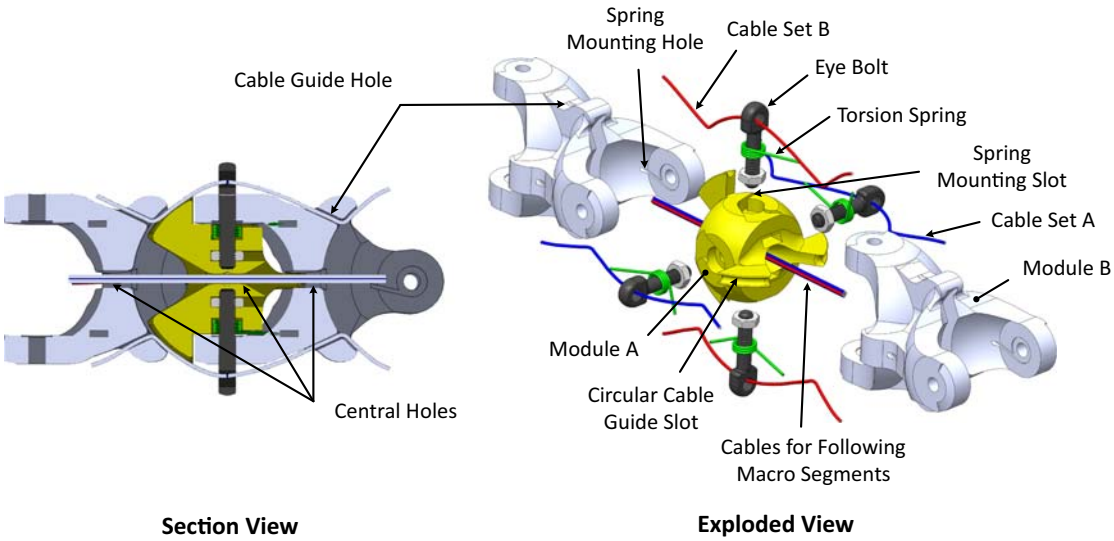

Fig. 8 The mechanical design of the segment assembly

Fig. 6(*b*). The two basic modules, module A and module B, were designed to achieve this functionality based on this idea.

As shown in Fig. 8, the main features of module A are the two sets of perpendicular mounting holes to mount the four eye bolts and the two sets of perpendicular circular cable guide slots to guide the two cable sets. Besides these main features, several specific design details should also be mentioned. The spring mounting slot is made to mount one leg of the torsion spring. The center hole is made to go through the cables for the following macro segments. Moreover, due to the rotation of module B with respect to module A, each set of circular cable guide slots is divided into two halves so that they will not block the center cables during motion.

Module B is designed to have the complementary mounting structures to module A. For instance, the cable guide hole on module B is made to work with the circular cable guide slot on module A to guide the cable to the next segment. Also, module B has a center hole to allow the cables for the next macro segment to pass through.

By designing module A and module B in such a way, the segment mechanism satisfies the necessary and sufficient conditions in the theorem and thus possesses the cable length invariance feature. Figure 9 shows how the segment assembly conforms to the mechanism in Fig. 6(*b*). As shown in Fig. 9, module A is essentially the rigid body O_2 with two half circles $\mathrm{Cir}_{O_2G_2P_3}$ and $\mathrm{Cir}_{O_2A_2P_2}$ in Fig. 6(*b*), and module B is essentially the rigid body consisting of half circles $\mathrm{Cir}_{O_1G_1P_3}$ and $\mathrm{Cir}_{O_2A_2P_3}$ in Fig. 6(*b*). However, to enhance the strength of module B, point P_3 is split to four separate points, namely, CA_1, CA_2, CB_1, and CB_2. Since CA_1 and CA_2 are both on the half circle $\mathrm{Cir}_{O_2G_2P_3}$, $g_{G_2CA_1}$ and $g_{H_2CA_2}$ are always complementary to each other during the rotation with respect to axis A_2B_2, which keeps $l(g_{G_2CA_1}) + l(g_{H_2CA_2})$ constant. Moreover, the cable segments from G_1 to CA_1 and from H_1 to CA_2 on module B are fixed cables, whose lengths are not affected by the joint motion. Therefore, the length of cable set A remains constant. Similarly, cable set B maintains the same length invariance property under joint motion. This justifies our design of the segment. It is worth noting that since the two rotation axes on module A are perpendicular to each other, the pitch bending is decoupled from the yaw bending. This beneficial feature facilitates the trajectory planning as well as controller design.

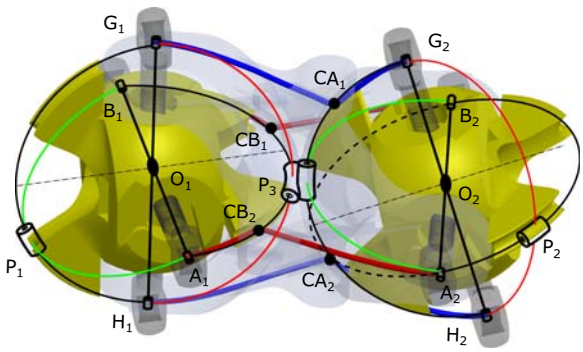

Fig. 9 The segment design capturing the mechanism in Fig. 6(*b*)

4.3 Macro Segment and Inter Macro Segment Cable Routing. RML tail is designed to support the multi macro segments feature, which is commonly observed in nature [32]. With this feature, the tail is able to exhibit more complex motions and thus increases the dexterity and versatility of the robot.

As shown in Fig. 10(*a*), the new macro segment can be added to the current tail by mounting an adapter module at the beginning of the new macro segment and routing the driving cables through the neutral path. The neutral path is defined as the line segments going through all of module A centers. For instance, the line segment connecting circle centers O_1 and O_2 in Fig. 9 is one part of the neutral path. These points are also depicted in Fig. 10. Since O_1 and O_2 are fixed points on module B, the neutral path consisting of these fixed distance line segments maintains a constant length during tail motion. Routing cables in such a way guarantee that the new macro segment cables are not affected by the motion of its previous macro segments. Figure 10(*a*) also shows how the adapter module distributes the center cables to outside by a section view.

4.4 Elastic Elements. Since each macro segment consists of more than two segments, there are more DOFs than actuators. Therefore, to make the system determinant, additional constraints are required. In the USRT and other hyper-redundant robots [17], these constraints are implemented by the elastic elements such as springs. The same idea is applied in the RML tail, which utilizes two types of springs—the torsional springs in module A serving as the basic elastic backbone of the tail and the extensional springs between adjacent eyebolts serving to compensate for the gravity, friction, and the stiffness differences of torsional springs due to manufacturing. The torsional springs are designed to have the same stiffness and their mounting positions are depicted in Fig. 8, in which four 90 deg right-hand torsion springs are used for each segment and mounted symmetrically on module A (a

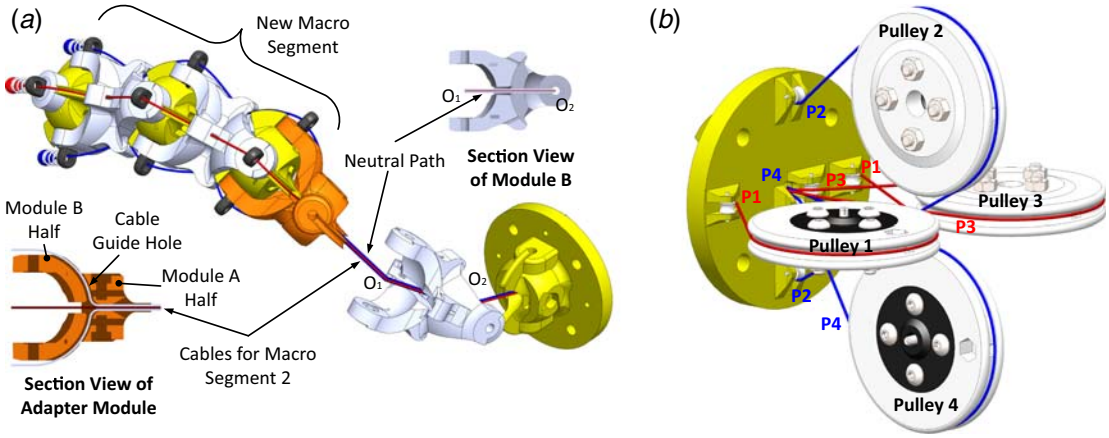

Fig. 10 (*a*) **Designs to achieve the multi macro segment feature and** (*b*) **the cable routing in the actuation module**

spring mounting slot) and module B (a corresponding spring mounting hole to mount the two spring legs). For the extensional springs, the stiffness is determined by experimentally adjusting the joint stiffness until they have the desired stiffness. The pretightening forces are determined by examining the different gravitational and frictional forces along the tail so that the tail maintains its natural position (the natural position is the pose when the yaw and pitch angles for each joint are all zero, i.e., the horizontal and straight pose) when the motors are turned off.

4.5 Actuation Module. Attributed to the unique cable routing profile formulated in this paper, only two motors are required for each macro segment. Therefore, the RML tail requires four actuators in total to drive the four sets of cables independently. Figure 10(*b*) shows the arrangement of the four pulleys and the corresponding cables' routings around the pulley. In Fig. 10(*b*), cables with the same label belong to the same cable set. For instance, the two horizontally aligned P1 labels indicate that they belong to the same cable set, i.e., the cable set B for macro segment 1 (driven by pulley 1); similarly, the cable with label P2 belongs to cable set A for macro segment 1 (driven by pulley 2); cable P3 belongs to cable set B for macro segment 2; and cable P4 belongs to cable set A for macro segment 2. The label colors are also consistent with the cable colors.

5 Kinematic, Dynamic Modeling, and Workspace Analysis

This section presents the kinematic and dynamic models of the RML tail and conducts a workspace analysis based on the static model. It is worth noting that due to the more generalized coordinates (12 in total) than actuators (4 in total), the system is essentially under actuated, for which the robot position and orientations cannot be determined by kinematics only. Dynamics has to be taken into account for even simple kinematic analysis. The models in this section are based on the assumptions that the cables are not stretchable and the cables perfectly follow their designed paths.

5.1 Kinematic Model. Figure 11 illustrates the kinematic configuration of the RML tail. $\sum S := (S, \mathbf{x}_s, \mathbf{y}_s, \mathbf{z}_s)$ is the body fixed frame of the housing module as well as the global frame, with its origin located at the intersection point of the four eye bolt axes, $\mathbf{z}_s$ being vertically up and $\mathbf{x}_s$ being horizontally forward. For the remaining moving links, the body fixed frames are all located at their COM (also the geometric center except link 6) and the orientations coincide with the global frame $\sum S$ at their initial position (when the tail stretches straight forward). The body fixed frame of link i ($i = 1, \ldots, 11$) is denoted as $\sum C_i := (C_i, \mathbf{x}_i, \mathbf{y}_i, \mathbf{z}_i)$, where point C_i is its COM. Therefore, the orientations of link i with respect to link $i-1$ and the base frame $\sum S$ are defined in Eq. (1), where $q_i \in [-q_{\text{lim}}, q_{\text{lim}}]$ is the rotation angle of the ith joint and $\mathbf{R}_Y(\cdot)$ and $\mathbf{R}_Z(\cdot)$ denote the elementary rotational matrices about y- and z-axis, respectively. $\mathcal{P} = \{1, 3, 5, 8, 10\}$ is the link set for pitch rotation while $\mathcal{Y} = \{2, 4, 6, 7, 9, 11\}$ is the link set for yaw rotation. $\mathbf{q} = [q_1, \ldots, q_{11}]^T$ is chosen to be the generalized coordinate.

$$ {}^{i-1}\mathbf{R}_i = \begin{cases} \mathbf{R}_Y(q_i), & i \in P \\ \mathbf{R}_Z(q_i), & i \in Y \end{cases}; \quad {}^{S}\mathbf{R}_i = \begin{cases} I, & i = 0 \\ {}^{S}\mathbf{R}_{i-1} \cdot {}^{i-1}\mathbf{R}_i, & i > 0 \end{cases} \tag{1} $$

Due to the circular cable guide slots, q_i has a fixed relationship with the cable shortening quantity, δ_i, with respect to the initial position of the ith joint, which is given in Eq. (2) where r is the radius of the circular cable guide slots. Based on the ith joint cable shortening length, δ_i, the overall cable shortening quantity, Δ_j, for jth pulley ($j = 1, \ldots, 4$) is also obtained as follows:

$$ q_i = \delta_i / r; \quad \Delta_j = \begin{cases} \delta_2 + \delta_4 + \delta_6, & j = 1 \\ \delta_1 + \delta_3 + \delta_5, & j = 2 \\ \delta_7 + \delta_9 + \delta_{11}, & j = 3 \\ \delta_8 + \delta_{10}, & j = 4 \end{cases} \tag{2} $$

By knowing the orientation of each link, the position vector ${}^{S}\mathbf{p}_i$ (or just $\mathbf{p}_i$ without left superscript to denote the vector in the global frame) of point C_i in the global frame $\sum S$ is obtained by Eq. (3), where $\mathbf{p}_{i-1,i}$ is the vector from point C_{i-1} to point C_i in frame $\sum S$. L is the distance between the two rotation axes in module B. $\mathbf{x}_i$ is the x base vector of frame $\sum C_i$ (the first column of ${}^{S}\mathbf{R}_i$). $\mathcal{Y}_s = \{2, 4, 9, 11\}$ is a subset of $\mathcal{Y}$.

$$ \mathbf{p}_i = \begin{cases} 0, & i = 0 \\ \mathbf{p}_{i-1} + \mathbf{p}_{i-1,i}, & i > 0 \end{cases}; \quad \mathbf{p}_{i-1,i} = \begin{cases} \mathbf{x}_i L/2, & i \in P \\ \mathbf{x}_{i-1} L/2, & i \in \mathcal{Y}_s \\ \mathbf{x}_5 L/2 + L_a \mathbf{x}_6, & i = 6 \\ L_b \mathbf{x}_6, & i = 7 \end{cases} \tag{3} $$

Besides the COM positions, the distances between adjacent eyebolts are also required to calculate the elastic forces introduced by the extension springs. For this purpose, the vector $\mathbf{d}_{s/l,i}$ is used to indicate the shorter/longer vector (when q_i is positive) associated with rotation q_i. For instance, as shown in Fig. 11, when q_8 is positive, the distance between the bottom two eyebolts is shorter than the distance between the two eyebolts on top. Therefore, the bottom vector is labeled as $\mathbf{d}_{s,8}$ and the top vector is denoted

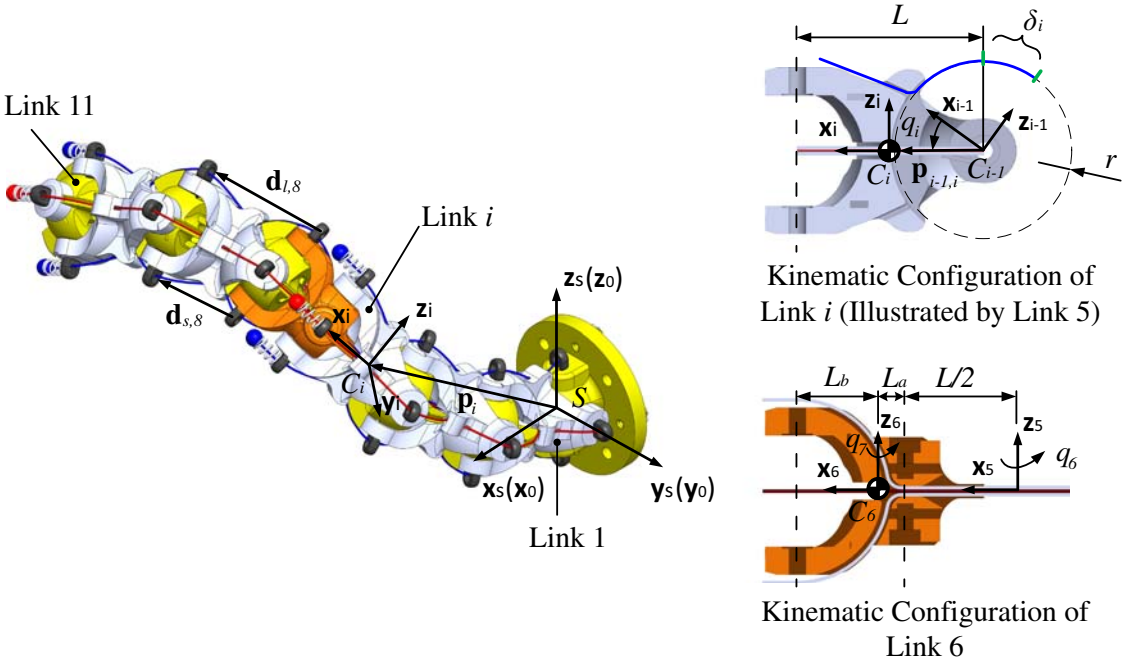

Fig. 11 Kinematic configuration of the RML tail

as $\mathbf{d}_{l,8}$. The $\mathbf{d}_{s/l,i}$ in frame $\sum C_i$ is obtained as follows:

$$\begin{cases} {}^i\mathbf{d}_{s,i} = L^i\mathbf{x}_i - r^i\mathbf{z}_i + r^i\mathbf{z}_{i-1}, & i \in P \\ {}^i\mathbf{d}_{l,i} = L^i\mathbf{x}_i + r^i\mathbf{z}_i - r^i\mathbf{z}_{i-1}, & i \in P \\ {}^i\mathbf{d}_{s,i} = K^i\mathbf{x}_{i-1} + r^i\mathbf{y}_i - r^i\mathbf{y}_{i-1}, & i \in Y \\ {}^i\mathbf{d}_{l,i} = K^i\mathbf{x}_{i-1} - r^i\mathbf{y}_i + r^i\mathbf{y}_{i-1}, & i \in Y \end{cases} \tag{4}$$

where

$$K = \begin{cases} L, & i \neq 7 \\ L_a + L_b, & i = 7 \end{cases} \tag{5}$$

For the purpose of dynamic modeling, the velocity, Jacobian matrices, and acceleration for each link are required. These terms may be obtained by differentiating the position relationships recursively, which yields the angular velocity $\boldsymbol{\omega}_i$ and linear velocity $\mathbf{v}_i$ of link i as given in Eqs. (6)–(8), where the tilde indicates the skew symmetric matrix of a vector and $\mathcal{P}_s = \{3, 5, 8, 10\}$ is a subset of $\mathcal{P}$.

$$\boldsymbol{\omega}_i = \begin{cases} \dot{q}_1\mathbf{y}_1, & i = 1 \\ \boldsymbol{\omega}_{i-1} + \dot{q}_i\mathbf{z}_i, & i \in Y \\ \boldsymbol{\omega}_{i-1} + \dot{q}_i\mathbf{y}_i, & i \in \mathcal{P}_s \end{cases} \tag{6}$$

$$\mathbf{v}_i = \begin{cases} 0, & i = 0 \\ \mathbf{v}_{i-1} + \mathbf{v}_{i-1,i}, & i > 0 \end{cases} \tag{7}$$

$$\mathbf{v}_{i-1,i} = \begin{cases} \tilde{\boldsymbol{\omega}}_i\mathbf{x}_i L/2, & i \in P \\ \tilde{\boldsymbol{\omega}}_{i-1}\mathbf{x}_{i-1} L/2, & i \in \mathcal{Y}_s \\ \tilde{\boldsymbol{\omega}}_5\mathbf{x}_5 L/2 + L_a\tilde{\boldsymbol{\omega}}_6\mathbf{x}_6, & i = 6 \\ L_b\tilde{\boldsymbol{\omega}}_6\mathbf{x}_6, & i = 7 \end{cases} \tag{8}$$

The corresponding Jacobian matrices $\mathbf{J}_{\omega,i}$ and $\mathbf{J}_{v,i}$ for angular and linear velocities are obtained by factoring out $\dot{q}_i$ from Eqs. (6)–(8), which yields

$$\mathbf{J}_{\omega,i} = \begin{cases} \mathbf{U}_{1,y}, & i = 1 \\ \mathbf{J}_{\omega,i-1} + \mathbf{U}_{i,z}, & i \in Y \\ \mathbf{J}_{\omega,i-1} + \mathbf{U}_{i,y}, & i \in \mathcal{P}_s \end{cases} \tag{9}$$

$$\mathbf{J}_{v,i} = \begin{cases} 0_{3\times 11}, & i = 0 \\ \mathbf{J}_{v,i-1} + \mathbf{J}_{v,i-1,i}, & i > 0 \end{cases} \tag{10}$$

$$\mathbf{J}_{v,i-1,i} = \begin{cases} -\tilde{\mathbf{x}}_i\mathbf{J}_{\omega,i}L/2, & i \in P \\ -\tilde{\mathbf{x}}_{i-1}\mathbf{J}_{\omega,i-1}L/2, & i \in \mathcal{Y}_s \\ -\tilde{\mathbf{x}}_5\mathbf{J}_{\omega,5}L/2 - L_a\tilde{\mathbf{x}}_6\mathbf{J}_{\omega,6}, & i = 6 \\ -L_b\tilde{\mathbf{x}}_6\mathbf{J}_{\omega,6}, & i = 7 \end{cases} \tag{11}$$

where $\mathbf{U}_{i,y}$ and $\mathbf{U}_{i,z}$ are the 3×11 zero matrix with the ith column being filled by $\mathbf{y}_i$ and $\mathbf{z}_i$, respectively. Then, the angular acceleration $\dot{\boldsymbol{\omega}}_i$ and linear acceleration $\dot{\mathbf{v}}_i$ are obtained by differentiating Eqs. (6)–(8), which are given as follows:

$$\dot{\boldsymbol{\omega}}_i = \begin{cases} \ddot{q}_1\mathbf{y}_1, & i = 1 \\ \dot{\boldsymbol{\omega}}_{i-1} + \ddot{q}_i\mathbf{z}_i + \dot{q}_i\tilde{\boldsymbol{\omega}}_i\mathbf{z}_i, & i \in Y \\ \dot{\boldsymbol{\omega}}_{i-1} + \ddot{q}_i\mathbf{y}_i + \dot{q}_i\tilde{\boldsymbol{\omega}}_i\mathbf{y}_i, & i \in \mathcal{P}_s \end{cases} \tag{12}$$

$$\dot{\mathbf{v}}_i = \begin{cases} 0, & i = 0 \\ \dot{\mathbf{v}}_{i-1} + \dot{\mathbf{v}}_{i-1,i}, & i > 0 \end{cases} \tag{13}$$

$$\dot{\mathbf{v}}_{i-1,i} = \begin{cases} (\tilde{\dot{\boldsymbol{\omega}}}_i\mathbf{x}_i + \tilde{\boldsymbol{\omega}}_i^2\mathbf{x}_i)L/2, & i \in P \\ (\tilde{\dot{\boldsymbol{\omega}}}_{i-1}\mathbf{x}_{i-1} + \tilde{\boldsymbol{\omega}}_{i-1}^2\mathbf{x}_{i-1})L/2, & i \in \mathcal{Y}_s \\ (\tilde{\dot{\boldsymbol{\omega}}}_5\mathbf{x}_5 + \tilde{\boldsymbol{\omega}}_5^2\mathbf{x}_5)L/2 + L_a(\tilde{\dot{\boldsymbol{\omega}}}_6\mathbf{x}_6 + \tilde{\boldsymbol{\omega}}_6^2\mathbf{x}_6), & i = 6 \\ L_b(\tilde{\dot{\boldsymbol{\omega}}}_6\mathbf{x}_6 + \tilde{\boldsymbol{\omega}}_6^2\mathbf{x}_6), & i = 7 \end{cases} \tag{14}$$

5.2 Dynamic Model. The dynamics is modeled based on the principle of virtual work as follows

$$\sum_{i=1}^{N}\left[\delta\mathbf{x}_i^T(\mathbf{F}_i - m_i\dot{\mathbf{v}}_i) + \delta\boldsymbol{\theta}_i^T(\mathbf{M}_i - \mathbf{I}_i\dot{\boldsymbol{\omega}}_i - \tilde{\boldsymbol{\omega}}_i\mathbf{I}_i\boldsymbol{\omega}_i)\right] = 0 \tag{15}$$

for an N body system, where $\mathbf{F}_i$ and $\mathbf{M}_i$ are the active forces on body i. $\mathbf{I}_i$ is the inertia matrix for body i and $\mathbf{v}_i$ and $\boldsymbol{\omega}_i$ are the linear and angular velocities. $\delta\mathbf{x}_i$ and $\delta\boldsymbol{\theta}_i$ are the linear and angular virtual displacements of body i. Substituting $\delta\mathbf{x}_i = \mathbf{J}_{v,i}\delta\mathbf{q}$ and $\delta\boldsymbol{\theta}_i = \mathbf{J}_{\omega,i}\delta\mathbf{q}$ and rearranging Eq. (15) by placing the actuation force on the left and

the other terms on the right yields

$$\sum_{i=1}^{N}(\mathbf{J}_{v,i}^{T}\mathbf{F}_{a,i}+\mathbf{J}_{\omega,i}^{T}\mathbf{M}_{a,i})=\sum_{i=1}^{N}\left[\mathbf{J}_{v,i}^{T}(\mathbf{F}_{l,i}-m_i\dot{\mathbf{v}}_i)+\mathbf{J}_{\omega,i}^{T}(\mathbf{M}_{l,i}-\mathbf{I}_i\dot{\boldsymbol{\omega}}_i-\tilde{\boldsymbol{\omega}}_i\mathbf{I}_i\boldsymbol{\omega}_i)\right] \tag{16}$$

$\mathbf{F}_{a,i}$ and $\mathbf{M}_{a,i}$ are the actuation forces and $\mathbf{F}_{l,i}$ and $\mathbf{M}_{l,i}$ account for all the nonactuated external forces including gravity, elastic force, friction, etc. Based on Eq. (16), the dynamic model of the RML tail is formulated as

$$\sum_{j=1}^{4}\mathbf{J}_{\Delta,j}^{T}\mathbf{t}=\sum_{i=1}^{11}(\boldsymbol{\tau}_{\text{inr},i}+\boldsymbol{\tau}_{\text{grv},i}+\boldsymbol{\tau}_{\text{tor},i}+\boldsymbol{\tau}_{\text{ext},i}+\boldsymbol{\tau}_{\text{dmp},i}) \tag{17}$$

where $\mathbf{t}=\begin{bmatrix}t_1 & t_2 & t_3 & t_4\end{bmatrix}^T$ and t_j is the cable tension of the jth pulley. The subscripts "inr," "grv," "tor," "ext," and "dmp" represent "inertia," "gravity," "torsional," "extension," and "damping" loadings, respectively. The damping loading accounts for all the equivalent frictions acting on the ith joint, including the highly nonlinear cable frictions. $\mathbf{J}_{\Delta,i}$ is the actuation Jacobian which may be computed by differentiating Eq. (2) and factoring out $\dot{\mathbf{q}}$. This gives the $\mathbf{J}_{\Delta,i}$'s jth row $\mathbf{j}_{\Delta,j}$ as

$$\mathbf{j}_{\Delta,j}=\begin{cases}r\mathbf{u}_{2,4,6}, & j=1\\ r\mathbf{u}_{1,3,5}, & j=2\\ r\mathbf{u}_{7,9,11}, & j=3\\ r\mathbf{u}_{8,10}, & j=4\end{cases} \tag{18}$$

where $\mathbf{u}$ is a 1×11 row vector with the entries indicated by the subscript being 1 and the rest entries being 0. The inertia and gravity loading are calculated straightforwardly using Eq. (19) where m_i and $\mathbf{I}_i$ are the mass and moment of inertia of link i measured in frame $\sum S$. The global inertia $\mathbf{I}_i$ may be calculated based on the local inertia ${}^{i}\mathbf{I}_i$ in frame $\sum C_i$ by $\mathbf{I}_i={}^{S}\mathbf{R}_i\cdot{}^{i}\mathbf{I}_i\cdot{}^{i}\mathbf{R}_S$. Depending on the link, m_i and $\mathbf{I}_i$ are chosen from the mass m_A and inertia $\mathbf{I}_A$ of module A, the mass m_B and inertia $\mathbf{I}_B$ of module B, or the mass m_{AB} and inertia $\mathbf{I}_{AB}$ of the adapter module.

$$\boldsymbol{\tau}_{\text{inr},i}+\boldsymbol{\tau}_{\text{grv},i}=\mathbf{J}_{v,i}^{T}m_i(\dot{\mathbf{v}}_i+g\mathbf{z}_s)+\mathbf{J}_{\omega,i}^{T}(\mathbf{I}_i\dot{\boldsymbol{\omega}}_i+\tilde{\boldsymbol{\omega}}_i\mathbf{I}_i\boldsymbol{\omega}_i) \tag{19}$$

Since the torsional spring loading $\boldsymbol{\tau}_{\text{tor},i}$ and the damping loading $\boldsymbol{\tau}_{\text{dmp},i}$ (the equivalent frictions are modeled as pure viscous frictions) are all functions of the joint variable q_i and $\dot{q}_i$, these two terms are calculated together as

$$\boldsymbol{\tau}_{\text{tor},i}+\boldsymbol{\tau}_{\text{dmp},i}=\mathbf{u}_i^{T}(2k_{\text{tor},i}q_i+c_{\text{dmp},i}\dot{q}_i) \tag{20}$$

where $k_{\text{tor},i}$ is the torsional spring stiffness and $c_{\text{dmp},i}$ is the damping coefficient. Again, $\mathbf{u}_i$ is the 1×11 row vector with the ith entry being 1 and the rest entries being 0.

The extension spring loading is derived from the virtual work of the elastic force, as shown in Eq. (21) where $\hat{\mathbf{d}}_{s,i}$ and $\hat{\mathbf{d}}_{l,i}$ are the unit vectors of $\mathbf{d}_{s,i}$ and $\mathbf{d}_{l,i}$, respectively. $k_{\text{ext},s,i}$, $L_{\text{ext},s,i}$, $k_{\text{ext},l,i}$, and $L_{\text{ext},l,i}$ are the shorter spring stiffness, shorter spring unloaded length, longer spring stiffness, and longer spring unloaded length, respectively.

$$\begin{aligned}\delta W_{\text{ext},i}=&\,k_{\text{ext},s,i}({}^{i}\mathbf{d}_{s,i}-L_{\text{ext},s,i})^{i}\hat{\mathbf{d}}_{s,i}\cdot\delta^{i}\mathbf{d}_{s,i}\\&k_{\text{ext},l,i}({}^{i}\mathbf{d}_{l,i}-L_{\text{ext},l,i})^{i}\hat{\mathbf{d}}_{l,i}\cdot\delta^{i}\mathbf{d}_{l,i}\end{aligned} \tag{21}$$

This gives the extension spring loading of link i as

$$\begin{aligned}\boldsymbol{\tau}_{\text{ext},i}=&\,\mathbf{u}_i^{T}k_{\text{ext},s,i}({}^{i}\mathbf{d}_{s,i}-L_{\text{ext},s,i})^{i}\hat{\mathbf{d}}_{s,i}^{T}\cdot{}^{i}\mathbf{e}_{s,i}\\&+\mathbf{u}_i^{T}k_{\text{ext},l,i}({}^{i}\mathbf{d}_{l,i}-L_{\text{ext},l,i})^{i}\hat{\mathbf{d}}_{l,i}^{T}\cdot{}^{i}\mathbf{e}_{l,i}\end{aligned} \tag{22}$$

where ${}^{i}\mathbf{e}_{s,i}$ and ${}^{i}\mathbf{e}_{l,i}$ are the terms by taking derivative of ${}^{i}\mathbf{d}_{s,i}$ and ${}^{i}\mathbf{d}_{l,i}$, respectively, as follows:

$$\begin{cases}{}^{i}\mathbf{e}_{s,i}=-r^{i}\tilde{\mathbf{y}}_i{}^{i}\mathbf{z}_{i-1}, & i\in P\\ {}^{i}\mathbf{e}_{l,i}=r^{i}\tilde{\mathbf{y}}_i{}^{i}\mathbf{z}_{i-1}, & i\in P\\ {}^{i}\mathbf{e}_{s,i}=-K^{i}\tilde{\mathbf{z}}_i{}^{i}\mathbf{x}_{i-1}+r^{i}\tilde{\mathbf{z}}_i{}^{i}\mathbf{y}_{i-1}, & i\in Y\\ {}^{i}\mathbf{e}_{l,i}=-K^{i}\tilde{\mathbf{z}}_i{}^{i}\mathbf{x}_{i-1}-r^{i}\tilde{\mathbf{z}}_i{}^{i}\mathbf{y}_{i-1}, & i\in Y\end{cases} \tag{23}$$

5.3 Workspace Analysis. In this section, two types of workspaces are investigated, namely, the end effector workspace and the COM workspace. The end effector workspace is necessary to illustrate the dexterity and mobility of the RML tail, and the COM workspace is depicted to show the variable COM which is desired in applications in which the tails are used as dynamical reaction appendages for mobile platforms. The end effector workspace is defined by all the points that the tail tip can reach in the 3D space (measured by the global frame $\sum S$). Similarly, the COM workspace consists of all the points in frame $\sum S$ that the COM of the RML tail can reach. The RML tail parameters are shown in Table 1 where m_S is the mass of the actuation module and the housing module.

Based on Eq. (3), the end effector position is $\mathbf{p}_{11}$. The overall center of mass $\mathbf{p}_{\text{COM}}$ is computed as

$$\mathbf{p}_{\text{COM}}=\frac{m_A\sum_{i\in\mathcal{P}}\mathbf{p}_i+m_B\sum_{i\in\{2,4,7,9,11\}}\mathbf{p}_i+m_{AB}\mathbf{p}_6}{5m_A+5m_B+m_{AB}} \tag{24}$$

By traversing a regular grid (joint angle range is $[-q_{\text{lim}}, q_{\text{lim}}]$) in the joint space, the corresponding workspace points are collected and their envelop boundaries are extracted. Figure 12 shows both the end effector workspace and the COM workspace where the thicker outer layer belongs to the end effector workspace and the thinner inner layer belongs to the COM workspace. The line segments from the origin to the end effector illustrate a specific configuration of the tail, where the first six represent the first macro segment and the second six represent the second macro segment. The diamond shape indicates the position of the COM for this configuration.

Tails with multi macro segments have the benefits of volumetric end effector workspace as well as volumetric COM workspace due to their abundant DOFs. In addition, serpentine tails usually have larger workspace than pendulum tails due to their ability to bend. These two benefits, as shown in Fig. 12, together make the RML tail suitable as both a flexible onboard manipulator and as a dynamical reaction appendage. Note that the COM workspace in Fig. 12 can be enlarged by adding more segments into each macro segment at the cost of more complex controls and the need for more powerful actuators.

6 Experimental Validation

A prototype was manufactured and integrated in order to verify the mechanism synthesized in this paper. Both static and dynamic experiments were conducted. The static experiments were used to validate the mechanism concept while the dynamic experiments evaluated the dynamic performance of the tail. It is worthy to note that since the prototype was developed as a proof-of-concept model focusing on the mechanism validation, high torque servos

Table 1 RML tail parameters

Variable	Value	Variable	Value
L	54 mm	m_A	26.7 g
L_a	6.32 mm	m_B	28 g
L_b	24.68 mm	m_{AB}	25.3 g
r	26 mm	m_S	1078.2 g
q_{lim}	30 deg	${}^{i}\mathbf{I}_A$	diag(1.26, 0.74, 0.74)10^{-5} kg m^2
$c_{\text{dmp},i}$	0.1 N m s rad^{-1}	${}^{i}\mathbf{I}_B$	diag(1.43, 2.21, 2.21)10^{-5} kg m^2
g	9.8 m s^{-2}	${}^{i}\mathbf{I}_{AB}$	diag(1.76, 1.73, 1.73)10^{-5} kg m^2

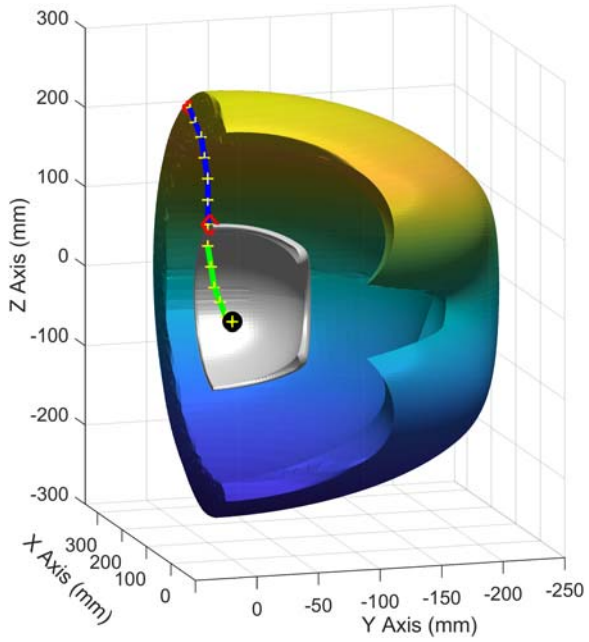

Fig. 12 Section view of the end effector workspace and the COM workspace of the RML tail

were selected for actuation, which limited the dynamic performances of the tail.

All of the tail's links including module A, module B, adapter module, and the housing module are printed using acrylonitrile butadiene styrene (ABS) plastic. The actuation module is built from laser cut ABS boards. Four HiTec HS-645MG Servos were chosen as the actuators due to their high torque (9.6 kg cm stall torque at 6.0 V) and an Arduino Uno was used as the microcontroller unit. To minimize cable elasticity, stainless steel nylon coated cable with 0.4 mm diameter was selected. 90 deg right-hand-type torsional springs were adopted so that there is no pretightening force for the natural position. For the extension springs, the stiffness and pretightening forces are determined by experimentally evaluating the joint bending so that every joint has the same bending angle along the tail (the last joint stiffness is treated as the desired stiffness, thus no external springs). Note that this design preference (uniform bending angle for each joint) is subject to change for other design purposes. The stiffness and pretightening forces of all springs used are measured and collected in Table 2.

6.1 Static Accuracy Measurements. The RML tail has two macro segments which make it as dexterous as most animal tails observed in nature. For each yaw or pitch bending, there are two shape modes, namely, the "C" shape and the "S" shape when the two macro segments bend in the same or different directions. This results in a total of four mode shapes for the entire tail, as shown in Fig. 14. It is worthy to note that due to the unique decoupled segment design, the yaw bending and pitch bending for each macro segment are actuated independently, which alleviates the control effort significantly. Figure 13(*b*) shows the rolling motion that can be achieved by combining the yaw and pitch bending motions.

The purpose of the static experiments is to validate the proposed mechanism and to evaluate the performance of the mechanical design, which is achieved through two sets of measurements. The first set measures the repeatability accuracy (10 times) of the two most important bending for tail applications: a 90 deg yaw bending and a 90 deg pitch bending. The shape accuracy (eyebolt positions) is measured manually by a coordinate board with an uncertainty of 1 mm, which is shown in Fig. 16(*a*). Figure 15 shows the comparison results between the measured shapes and the simulated shape in MATLAB. The simulated shapes are obtained via the dynamic simulations when the tail becomes stable. The

Table 2 RML tail elastic elements' properties

Variable	Type	Stiffness (N m rad^{-1})/(N m^{-1})	Pretightening torque (N m)/ force (N)
$k_{\text{tor},i}$	Tor., 90 deg right hand	0.0241	0
$k_{\text{ext},s,\ i} = k_{\text{ext},l,\ i}$, $i = 2, 4, 6, 7, 9$, respectively	Ext.	318.2, 92.5, 151.6, 183.1, 51.6	8.34, 1.08, 3.09, 3.30, 1.65
$k_{\text{ext},l,\ i}$, $i = 1, 3, 5, 8$, respectively	Ext.	401.6, 281.6, 197.6, 129.0	12.59, 7.97, 4.68, 2.58
$k_{\text{ext},s,\ i}$, $i = 1, 3, 5, 8$, respectively	Ext.	144.1, 44.1, 53.9, 111.4	2.08, 1.12, 1.71, 1.89

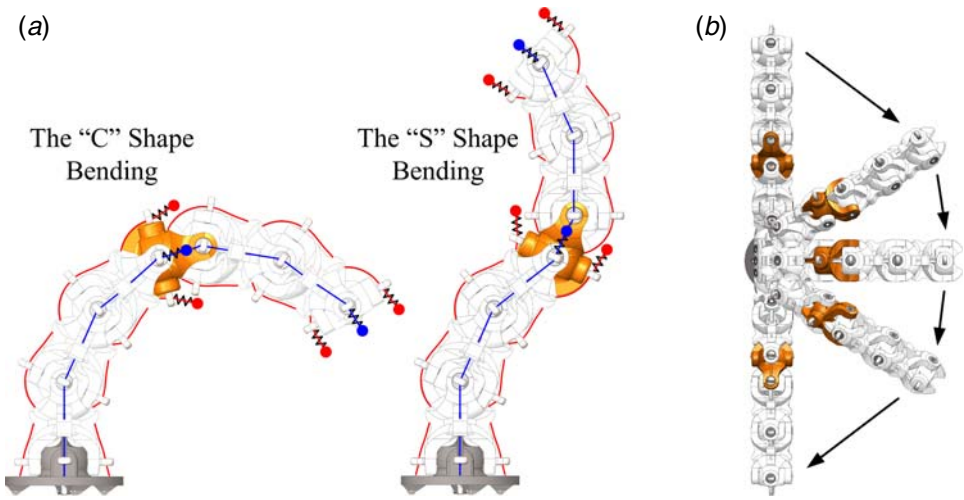

Fig. 13 (*a*) The two shapes for each bending and (*b*) combining yaw and pitch bending to achieve rolling motion (cables and some eyebolts are hidden for clarity)

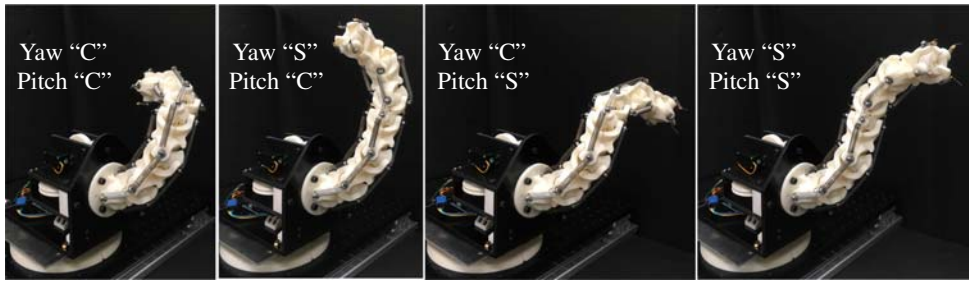

Fig. 14 Multimode shapes show the dexterity of the RML tail

experimental curve is reported by mean values along with their corresponding 95% confidence region (also called error ellipse) based on two-dimensional normal distribution assumption (note that the two dimensions are not uncorrelated).

By comparing the experimental measurements, the yaw bending has an average of 3.87 mm repetitive positioning accuracy of the seven eyebolts while the pitch bending has a larger average of 8.22 mm. This is reflected in Figs. 15(*a*) and 15(*b*) such that the yaw bending has a more uniform bending along the tail than the pitch bending. Specifically, the third eyebolt on the pitch bending curve shows a smaller bending angle than others (note that the fourth eyebolt itself does not have pitch joint due to the adapter module, thus no bending), which is believed to be due to the cable Coulomb friction neglected in the dynamic model. By comparing the uncertainty of each eyebolt along the tail, both Figs. 15(*a*) and 15(*b*) illustrate that the uncertainty increases as the eyebolt is away from the tail base. By comparing the simulated shapes and the measured shapes, the experimental yaw bending has a maximal deviation of 11.2 mm from the simulated shape while the experimental pitch bending has a maximal deviation of 17.3 mm from the simulated shape.

The second set of measurements measures the four mode shapes in Fig. 14. Stereo camera Kinect V2 (with a precision of 1.5 mm) is used to obtain the spatial coordinates of the eyebolts. Figure 16(*b*) shows how the Kinect camera is implemented in the experimental setup. Ten repetitive measurements for each mode shape are conducted to obtain the statistical information. In the same as the first set of measurement, the experimental poses are plotted by the mean joint positions along with their corresponding 95% confidence region (also called error ellipsoid) based on three-dimensional normal distribution assumption. Similarly, the three dimensions are not uncorrelated. Note that the raw data only provide the eyebolt positions. The joint positions are calculated and reconstructed via inverse kinematics.

Figure 17 shows the four typical spatial mode shapes from the second set of measurements, along with the error ellipsoid of each joint position. By observing the ellipsoid orientations, it was found that most of the ellipsoids' long axes are approximately located on the horizontal plane (*XY* plane), which implies that the horizontal direction causes the main uncertainty. Two sources are believed to be mainly responsible for this error distribution: the relatively large depth measurement uncertainty (measured from the $+Y$ direction) of the Kinect V2 camera and the relatively larger horizontal motion uncertainty (compared to the vertical motion uncertainty) of the tail. The largest distance error of each pose is found at the tip joint, which are 16.2 mm for the Yaw "C" Pitch "C" mode shape (denoted by CC for short, same rule applies to the other mode shapes), 19.1 mm for the SC mode shape, 16.9 mm for the CS mode shape, and 22.9 mm for the SS mode shape. Simulation results are also reported in Fig. 17, which show close results to the experiments. The maximum distance differences (joint positions) of the simulations from the experiments are reported as 9.45 mm for the CC mode shape, 7.26 mm for the SC mode shape, 9.42 mm for the CS mode shape, and 14.5 mm for the SS mode shape. Note that the four poses in Fig. 17 are not necessarily the same as the four poses as shown in Fig. 14. For each mode shape, the pose was selected by mainly considering the operational convenience and the presentation clarity. The ten repetitive tests for each pose always use the same pitch and yaw rotation angles.

6.2 Dynamic Performance Evaluations. Dynamic experiments were also conducted to evaluate the performance of the RML tail, which is achieved by measuring the generated forces and moments on the base. The forces are measured by a 6-axis load cell (SRI M3716B) with maximum nonlinearity of 0.5% of the measurement range. The tested trajectory is a simple point-to-point (from −90 deg to 90 deg) yaw bending of 180 deg in 0.75 s.

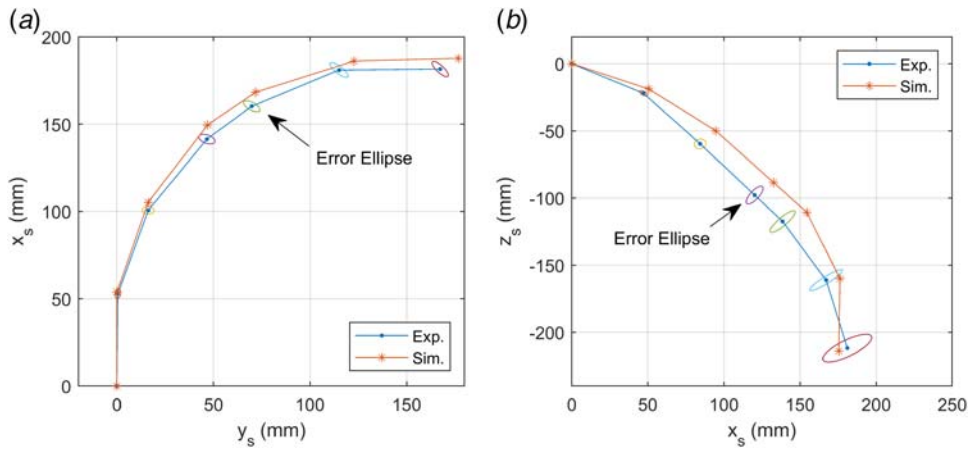

Fig. 15 Simulated and experimental shape measurements for (*a*) yaw bending of 90 deg and (*b*) pitch bending of 90 deg. The simulations were carried out in MATLAB with a multibody dynamics toolbox developed in the Robotics and Mechatronics Lab [33].

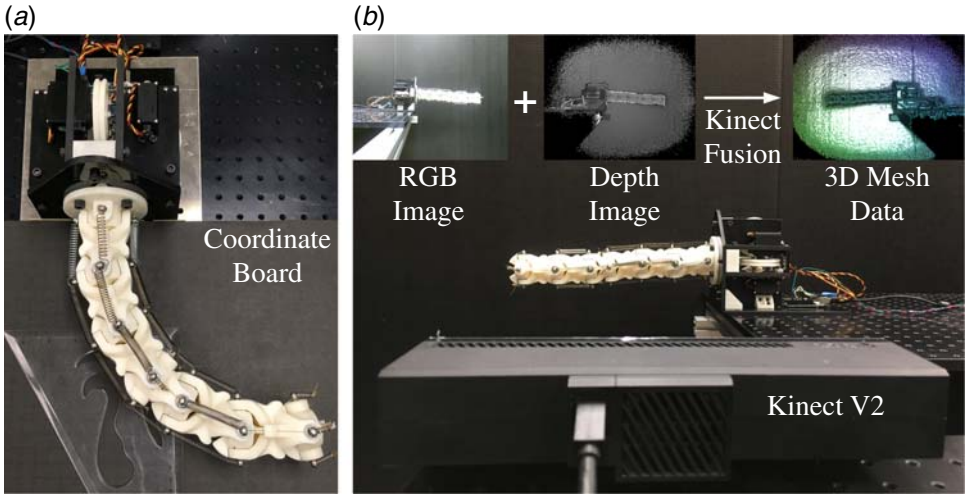

Fig. 16 Two implemented measurement techniques: (*a*) the coordinate board and (*b*) the Kinect V2 stereo camera system

On the servo side, this trajectory is equivalent to a rotation of 78 deg (the pulley diameter is 60 mm) in 0.75 s for pulley 1 and pulley 3.

Dynamic performances are also evaluated by simulations implemented in MATLAB. Due to the system's under-actuation feature, the input-to-output feedback linearization controller [34] is implemented to track the same trajectory as in the experiments. For better presentation, the dynamic model in Eq. (17) is written in the standard form as

$$\mathbf{M}\ddot{\mathbf{q}} + \mathbf{C} = \mathbf{B}\mathbf{t} \tag{25}$$

where $\mathbf{M}$ is the system inertia matrix, $\mathbf{B}$ is the actuation Jacobian, and $\mathbf{C}$ is the coupling matrix. $\mathbf{M}$, $\mathbf{B}$, and $\mathbf{C}$ are calculated by Eqs. (26) and (27), where $\boldsymbol{\tau}_{\text{gnl}}(\mathbf{q}, \dot{\mathbf{q}}, \ddot{\mathbf{q}})$ is the generalized dynamic loading vector.

$$\mathbf{M} = \sum_{i=1}^{11} (\mathbf{J}_{v,i}^T m_i \mathbf{J}_{v,i} + \mathbf{J}_{\omega,i}^T \mathbf{I}_i \mathbf{J}_{\omega,i}) \tag{26}$$

$$\mathbf{B} = \sum_{j=1}^{4} \mathbf{J}_{\Delta,j}^T; \quad \mathbf{C} = \boldsymbol{\tau}_{\text{gnl}}(\mathbf{q}, \dot{\mathbf{q}}, 0) \tag{27}$$

$$\boldsymbol{\tau}_{\text{gnl}}(\mathbf{q}, \dot{\mathbf{q}}, \ddot{\mathbf{q}}) = \sum_{i=1}^{11} (\boldsymbol{\tau}_{\text{inr},i} + \boldsymbol{\tau}_{\text{grv},i} + \boldsymbol{\tau}_{\text{tor},i} + \boldsymbol{\tau}_{\text{ext},i} + \boldsymbol{\tau}_{\text{dmp},i}) \tag{28}$$

For the tested trajectory, the output $\mathbf{h}$ and reference $\mathbf{h}_d$ are selected as

$$\mathbf{h} = \begin{bmatrix} q_1 + q_3 + q_5 \\ q_2 + q_4 + q_6 \\ q_8 + q_{10} \\ q_7 + q_9 + q_{11} \end{bmatrix}; \quad \mathbf{h}_d(t) = \begin{bmatrix} 0 \\ 0.6\pi t/0.75 - 0.3\pi \\ 0 \\ 0.6\pi t/0.75 - 0.3\pi \end{bmatrix} \tag{29}$$

where t is the time variable. Then, the closed loop control law is formulated as in Eq. (30) where $\mathbf{J}_h = \partial\mathbf{h}/\partial\mathbf{q}$ is the output Jacobian, and $\mathbf{K}_p$ and $\mathbf{K}_d$ are two symmetric positive definite matrices. Note that although the control law in Eq. (30) generates satisfying control performance in the simulation, the controller may be undermined by model uncertainties in practical application cases.

$$\mathbf{t} = (\mathbf{J}_h\mathbf{M}^{-1}\mathbf{B})^{-1}[\mathbf{J}_h\mathbf{M}^{-1}\mathbf{C} + \ddot{\mathbf{h}}_d + \mathbf{K}_p(\mathbf{h}_d - \mathbf{h}) + \mathbf{K}_d(\dot{\mathbf{h}}_d - \dot{\mathbf{h}})] \tag{30}$$

Figure 18 demonstrates the experimental data collected from the load cell and the simulated results from MATLAB. Note that the forces in Fig. 18 are the reaction forces measured from the base and the

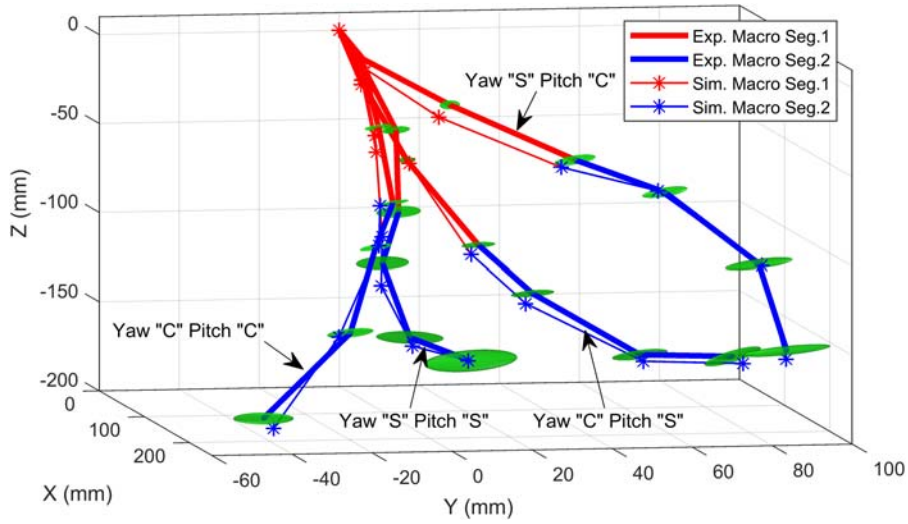

Fig. 17 3D measurements of four typical poses with uncertainty ellipsoids. The simulations were carried out in MATLAB with a multibody dynamics toolbox developed in the Robotics and Mechatronics Lab [33].

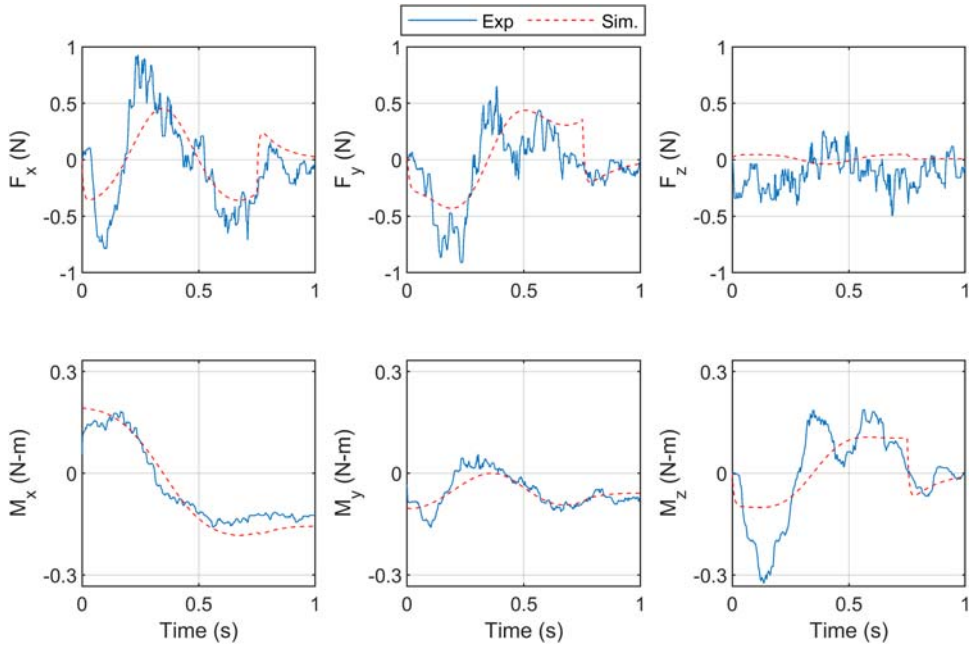

Fig. 18 Simulated and experimental loading for yaw bending of 180 deg in 0.75 s. The simulations were carried out in MATLAB with a multibody dynamics toolbox developed in the Robotics and Mechatronics Lab [33].

gravity is zeroed out, i.e., F_z is shifted by the gravity offset. Overshoots and fluctuations are observed from the experimental measurements in comparison with the simulated data, which are believed to result from model uncertainty, external disturbance, and the controller differences between simulations and experiments. In particular, a torque controller based on feedback linearization was adopted in the simulations, which has taken the dynamics of springs into account, while the prototype adopted a simple proportional integral differential (PID) position controller inside the servo motors. This resulted in the smooth reaction force behavior in simulations, which suggests the necessity of replacing the current built-in position controller with a robust model-based torque controller (for this purpose, the motors should be changed as well) for future work. However, it can be recognized that the simulations share similar trends with the experiments. Due to the smaller size and scale of the robotic tail and the use of less powerful motors, the peak angular loading is measured as 0.32 N m (M_z) in comparison to the reported 1.8 Nm for the DMST [20] and 2.7 Nm for the USRT [21].

7 Conclusion

For a cable-driven universal joint, the cable length invariance property is a preferable feature as it can lead to convenience in control, improvement of reliability, and simplicity in actuation. To achieve this goal, a theoretical mechanism synthesis process based on a spherical geometry assumption is first conducted. The main theorem demonstrated that the critical condition for realizing cable length invariance is to let the cables pass through the pivots of the two rotation axes of the universal joint. Based on this conclusion, the RML tail was designed, manufactured, and integrated. The new tail includes two independent macro segments (2 DOF for each) to generate more complex shapes (4 DOF in total), which help to enhance the dexterity and versatility of the robot. In addition, the pitch bending and yaw bending of the tail are decoupled due to the perpendicular joint axes. These beneficial features endow the RML tail with the advantages of fewer actuators, simpler controls, and a more robust structure. Kinematic and dynamic models were then derived to validate these characteristics. The workspace analysis showed that the RML tail has a much larger workspace than the traditional pendulum tail. In addition, two experiments focusing on static and dynamic behaviors of the tail were also conducted to validate the mechanism and evaluate the new tail's performance. The repeatability tests showed that the tail has an average of 3.87 mm repetitive positioning accuracy for 90 deg yaw bending and an average of 8.22 mm accuracy for 90 deg pitch bending. The dynamic experiments validated the RML tail dynamic model and illustrated similar behaviors with the simulations.

It is also worth noting that the mechanism synthesized in this paper has potential use in general applications such as tendon driven 2-DOF robotic joints (wrist, ankle, and pelvis) and flexible manipulators. However, since the work in this paper is based on the spherical geometry assumption, more general outer surfaces (such as ellipsoid or hyperboloid) and cable routing possibilities (for instance, the cable guiding grooves) will be considered to yield a more general cable length invariant design rule for the universal joint. After the general rule for universal joint is found, further investigations on other primitive joints (such as the Π, S joint, etc. Note that the R joint case is solved in the example of the DMST) should be conducted. Finally, a collection of rules to achieve cable invariance property might be carried out, as shown in Ref. [35]. For more complicated joint cases, calculus of variations might be used to compute the cable length.

Acknowledgment

This material is partially based upon work supported by the National Science Foundation (NSF) under Grant No. 1906727.

References

[1] Proske, U., 1980, "Energy Conservation by Elastic Storage in Kangaroos," Endeavour, **4**(4), pp. 148–153.
[2] Wilson, A. M., Lowe, J. C., Roskilly, K., Hudson, P. E., Golabek, K. A., and McNutt, J. W., 2013, "Locomotion Dynamics of Hunting in Wild Cheetahs," Nature, **498**(7453), pp. 185–189.
[3] Sfakiotakis, M., Lane, D. M., and Davies, J. B. C., 1999, "Review of Fish Swimming Modes for Aquatic Locomotion," IEEE J. Oceanic Eng., **24**(2), pp. 237–252.
[4] Young, J. W., Russo, G. A., Fellmann, C. D., Thatikunta, M. A., and Chadwell, B. A., 2015, "Tail Function During Arboreal Quadrupedalism in Squirrel Monkeys (*Saimiri boliviensis*) and Tamarins (*Saguinus oedipus*)," J. Exp. Zool. Part A, **323**(8), pp. 556–566.

[5] Jusufi, A., Kawano, D. T., Libby, T., and Full, R. J., 2010, "Righting and Turning in Mid-Air Using Appendage Inertia: Reptile Tails, Analytical Models and Bio-Inspired Robots," Bioinspir. Biomim., **5**(4), p. 045001.
[6] Libby, T., Moore, T. Y., Chang-Siu, E., Li, D., Cohen, D. J., Jusufi, A., and Full, R. J., 2012, "Tail-Assisted Pitch Control in Lizards, Robots and Dinosaurs," Nature, **481**(7380), p. 181.
[7] Patel, A., and Braae, M., 2013, "Rapid Turning at High-Speed: Inspirations From the Cheetah's Tail," IEEE/RSJ International Conference on Intelligent Robots and Systems, Tokyo, Japan, Nov. 3–7, pp. 5506–5511.
[8] Patel, A., and Braae, M., 2014, "Rapid Acceleration and Braking: Inspirations From the Cheetah's Tail," IEEE International Conference on Robotics and Automation, Hong Kong, China, May 31–Jun. 7, pp. 793–799.
[9] Rone, W., and Ben-Tzvi, P., 2016, "Dynamic Modeling and Simulation of a Yaw-Angle Quadruped Maneuvering With a Planar Robotic Tail," J. Dyn. Syst. Meas. Control, **138**(8), p. 084502.
[10] Liu, Y., and Ben-Tzvi, P., 2018, "Dynamic Modeling of a Quadruped With a Robotic Tail Using Virtual Work Principle," Proceedings of the IDETC/CIE, Quebec City, Canada, Aug. 26–29, p. V05BT07A021, ASME Paper No. DETC2018-86048.
[11] Patel, A., and Boje, E., 2015, "On the Conical Motion of a Two-Degree-of-Freedom Tail Inspired by the Cheetah," IEEE Trans. Rob., **31**(6), pp. 1555–1560.
[12] Zhao, J., Zhao, T., Xi, N., Mutka, M. W., and Xiao, L., 2015, "MSU Tailbot: Controlling Aerial Maneuver of a Miniature-Tailed Jumping Robot," IEEE/ASME Trans. Mechatron., **20**(6), pp. 2903–2914.
[13] Chang-Siu, E., Libby, T., Tomizuka, M., and Full, R. J., 2011, "A Lizard-Inspired Active Tail Enables Rapid Maneuvers and Dynamic Stabilization in a Terrestrial Robot," IEEE/RSJ International Conference on Intelligent Robots and Systems, San Francisco, CA, Sept. 25–30, pp. 1887–1894.
[14] Liu, G. H., Lin, H. Y., Lin, H. Y., Chen, S. T., and Lin, P. C., 2014, "A Bio-Inspired Hopping Kangaroo Robot With an Active Tail," J. Bionic Eng., **11**(4), pp. 541–555.
[15] Briggs, R., Lee, J., Haberland, M., and Kim, S., 2012, "Tails in Biomimetic Design: Analysis, Simulation, and Experiment," IEEE/RSJ International Conference on Intelligent Robots and Systems, Vilamoura, Portugal, Oct. 7–12, pp. 1473–1480.
[16] De, A., and Koditschek, D. E., 2015, "Parallel Composition of Templates for Tail-Energized Planar Hopping," IEEE International Conference on Robotics and Automation, Seattle, WA, May 26–30, pp. 4562–4569.
[17] Hannan, M. W., and Walker, I. D., 2003, "Kinematics and the Implementation of an Elephant's Trunk Manipulator and Other Continuum Style Robots," J. Rob. Syst., **20**(2), pp. 45–63.
[18] Moses, M. S., Kutzer, M. D. M., Ma, H., and Armand, M., 2013, "A Continuum Manipulator Made of Interlocking Fibers," IEEE International Conference on Robotics and Automation, Karlsruhe, Germany, May 6–10, pp. 4008–4015.
[19] Kim, Y. J., Cheng, S., Kim, S., and Iagnemma, K., 2014, "A Stiffness-Adjustable Hyperredundant Manipulator Using a Variable Neutral-Line Mechanism for Minimally Invasive Surgery," IEEE Trans. Rob., **30**(2), pp. 382–395.
[20] Saab, W., Rone, W. S., and Ben-Tzvi, P., 2018, "Discrete Modular Serpentine Robotic Tail: Design, Analysis and Experimentation," Robotica, **36**(7), pp. 994–1018.
[21] Rone, W. S., Saab, W., and Ben-Tzvi, P., 2018, "Design, Modeling, and Integration of a Flexible Universal Spatial Robotic Tail," ASME J. Mech. Rob., **10**(4), p. 041001.
[22] Saab, W., Rone, W. S., Kumar, A., and Ben-Tzvi, P., 2019, "Design and Integration of a Novel Spatial Articulated Robotic Tail," IEEE/ASME Trans. Mechatron., **24**(2), pp. 434–446.
[23] Rone, W. S., Liu, Y., and Ben-Tzvi, P., 2019, "Maneuvering and Stabilization Control of a Bipedal Robot With a Universal-Spatial Robotic Tail," Bioinspir. Biomim., **14**(1), p. 016014.
[24] Rone, W. S., and Ben-Tzvi, P., 2012, "Continuum Manipulator Statics Based on the Principle of Virtual Work," Proceedings of the IMECE, Houston, TX, Nov. 9–15, pp. 321–328, ASME Paper No. IMECE2012-87675.
[25] Saab, W., Rone, W. S., and Ben-Tzvi, P., 2018, "Robotic Tails: A State-of-the-art Review," Robotica, **36**(9), pp. 1263–1277.
[26] Lim, W. B., Yeo, S. H., Yang, G., and Mustafa, S. K., 2009, "Kinematic Analysis and Design Optimization of a Cable-Driven Universal Joint Module," IEEE/ASME International Conference on Advanced Intelligent Mechatronics, Singapore, Singapore, July 14–17, pp. 1933–1938.
[27] Tang, L., Wang, J., Zheng, Y., Gu, G., Zhu, L., and Zhu, X., 2017, "Design of a Cable-Driven Hyper-Redundant Robot With Experimental Validation," Int. J. Adv. Rob. Syst., **14**(5), p. 1729881417734458.
[28] Yigit, C. B., and Boyraz, P., 2017, "Design and Modelling of a Cable-Driven Parallel-Series Hybrid Variable Stiffness Joint Mechanism for Robotics," Mech. Sci., **8**(1), pp. 65–77.
[29] Kim, Y. J., 2017, "Anthropomorphic Low-Inertia High-Stiffness Manipulator for High-Speed Safe Interaction," IEEE Trans. Rob., **33**(6), pp. 1358–1374.
[30] Liu, Y., Kong, M., Wan, N., and Ben-Tzvi, P., 2018, "A Geometric Approach to Obtain the Closed-Form Forward Kinematics of H4 Parallel Robot," ASME J. Mech. Rob., **10**(5), p. 051013.
[31] Huang, T., Li, Z., Li, M., Chetwynd, D. G., and Gosselin, C. M., 2004, "Conceptual Design and Dimensional Synthesis of a Novel 2-DOF Translational Parallel Robot for Pick-and-Place Operations," ASME J. Mech. Des., **126**(3), pp. 449–455.
[32] Patel, A., Stocks, B., Fisher, C., Nicolls, F., and Boje, E., 2017, "Tracking the Cheetah Tail Using Animal-Borne Cameras, GPS, and an IMU," IEEE Sens Lett., **1**(4), pp. 1–4.
[33] Wang, J., Kamidi, V., and Ben-Tzvi, P., 2018, "A Multibody Toolbox for Hybrid Dynamic System Modeling Based on Nonholonomic Symbolic Formalism," Proceedings of the DSCC, Atlanta, GA, Sept. 30–Oct. 3, pp. V003T29A003, ASME Paper No. DSCC2018-9000.
[34] Isidori, A., 1995, *Nonlinear Control Systems*, Springer, Berlin.
[35] Caro, S., Khan, W. A., Pasini, D., and Angeles, J., 2010, "The Rule-Based Conceptual Design of the Architecture of Serial Schönflies-Motion Generators," Mech. Mach. Theory, **45**(2), pp. 251–260.